

HARD X-RAY AND MICROWAVE OBSERVATIONS OF MICROFLARES

JIONG QIU,^{1,2} CHANG LIU,² DALE E. GARY,² GELU M. NITA,² AND HAIMIN WANG^{1,2}

Received 2004 March 22; accepted 2004 May 5

ABSTRACT

In this paper, we study solar microflares using the coordinated hard X-ray and microwave observations obtained by the *Reuven Ramaty High Energy Solar Spectroscopic Imager (RHESSI)* during its open-shutter operation mode and the Owens Valley Solar Array (OVSA). The events in our study are selected in the energy range of 12–25 keV and are relatively large microflares with an average *GOES* soft X-ray incremental flux at the B2.0 level. A total of 760 microflares are identified from the *RHESSI* burst catalog. Of the 200 microflares that fall into the OVSA observing window, about 40% are detected in microwaves. Using these hundreds of events as samples, we study the event distribution with respect to the flux, the solar activity, and active regions, in comparison with flares of larger scales. Nonthermal properties of microflares are investigated through spectral analysis of X-rays and microwaves. (1) We find that the event frequency distribution with respect to the *RHESSI* peak count rates at 12–25 keV can be accurately described with a power-law function down to 8 counts s⁻¹, the power-law index being 1.75 ± 0.03 , consistent with previous studies. (2) Similar to large flares, the occurrence rate of microflares is correlated with solar activity. The studied samples of microflares are mostly produced by active regions, as suggested by the large percentage of events detected by OVSA, which observes target active regions. However, all active regions do not have equal productivity, and certain active regions are a lot more productive than other regions. (3) While some large and complex active regions are predominantly productive in both very weak and strong events, we also find an active region that produces many microflares and C-class events but does not produce powerful events. (4) Analysis of energy-dependent time profiles suggests that there is a pronounced temporal correlation between the time derivative of soft X-rays and 14–20 keV hard X-rays, i.e., the Neupert effect, in about one-half the studied events. (5) Albeit small, many microflares exhibit hard X-ray emission at over 10 keV and microwave emission at around 10 GHz. Spectral analysis in these two wavelengths corroborates the nonthermal nature of these emissions. (6) In a limited number of samples, the *RHESSI* spectral fitting yields a photon spectral index of 4.5–7, and microwave spectral analysis on the same events shows that the power-law index of the electron spectrum is in the range of 2–5. The discrepancy in the electron spectrum index derived from hard X-rays and microwaves is substantially greater than previously reported in big flares, hinting at the existence of high-energy, microwave-emitting electrons that have a much hardened spectrum compared with electrons emitting hard X-rays.

Subject headings: Sun: activity — Sun: flares — Sun: magnetic fields — Sun: radio radiation —
Sun: X-rays, gamma rays

1. INTRODUCTION

High-quality observational studies of small-scale solar transient brightenings or bursts are important to elucidate the mechanisms of coronal heating (Zirker 1993). Observations of these events, including microflares that refer to small-scale reconnection events, have been studied in a broad range across the electromagnetic spectrum in both the quiet Sun and active regions (Porter et al. 1987; Canfield & Metcalf 1987; Simnett et al. 1989; Shimizu 1995; Nitta 1997; Gary et al. 1997; Krucker et al. 1997; Wang et al. 1999; Qiu et al. 1999; Aschwanden 1999; Krucker & Benz 2000; Berghmans et al. 2001; Shimizu et al. 2002). An issue of interest concerns whether these transient solar energy releases on small scales are primarily nonthermal in nature. Observations in hard X-ray and radio wavelengths have shown evidence of nonthermal components in some events. Using a balloon-borne instrument,

Lin et al. (1984) first discovered hard X-ray microflares that emit at over 25 keV, and their photon spectra exhibit a power-law distribution with a power-law index of 4–6. The observations hence suggest that these greater than 25 keV bursts are of nonthermal origin and electron acceleration takes place in these small-scale events as well. In search of the nonthermal (gyrosynchrotron) microwave counterpart of active region soft X-ray transients (Shimizu et al. 1994; Shimizu 1995), some studies yielded inconclusive results (Bastian 1991; White et al. 1995), but others (Gopalswamy et al. 1994; Gary et al. 1997) found events in which microwave emission correlated with the soft X-ray transients is definitely a result of a nonthermal population of electrons.

The recently launched *Reuven Ramaty High Energy Solar Spectroscopic Imager (RHESSI)*, with its unrivaled high sensitivity to greater than 3 keV photons and spectral resolution of 1 keV, provides a unique opportunity to study both the high-temperature and nonthermal components of microflares in a continuous spectrum (Lin et al. 2002). The first light results of *RHESSI* microflare observations were presented by Benz & Grigis (2002) and Krucker et al. (2002). Liu et al. (2004) and Garaimov et al. (2003) compared *RHESSI* microflares with observations in H α and 17 GHz microwaves, respectively.

¹ Big Bear Solar Observatory, New Jersey Institute of Technology, 40386 North Shore Lane, Big Bear City, CA 92314-9672; qiu@bbso.njit.edu.

² Center for Solar-Terrestrial Research, Physics Department, New Jersey Institute of Technology, 323 Dr. Martin Luther King, Jr. Boulevard, Newark, NJ 07102-1982.

These studies show that the temporal, spatial, spectral, and magnetic properties of active region microflares are similar to larger flares, in agreement with the original definition that microflares are small-scale reconnection events (Parker 1983). More than 10 events are studied in these papers, which demonstrate a clearly distinguishable nonthermal component from 8 to 15 keV.

The *RHESSI* database, which contains thousands of solar X-ray bursts recorded each year, is yet to be substantially explored. This microflare study covers several hundred microflares registered during the *RHESSI* open-shutter observing mode from 2002 May–September. Instruments and data selection principles are described in § 2. In this paper, we present the results of the first-stage study in two parts. With the hundreds of events, we revisit statistical characteristics that have been extensively addressed in the past studies, such as the general properties, number distribution, and solar disk distribution of the hard X-ray microflares detected by the instrument with unprecedented sensitivity (§ 3). Because of the high sensitivity of microwave observations to nonthermal electrons, we also identify microwave emissions in microflares using coordinated Owens Valley Solar Array (OVSA) observations to investigate the nonthermal properties of microflares (§§ 3 and 4). The results are summarized and discussed in view of previous studies in the last section.

2. OBSERVATIONS

2.1. Instruments

RHESSI was launched in 2002 February to observe solar flares in the energy range from 3 keV to 17 MeV with an unprecedented energy resolution of 1 keV at low energies (Lin et al. 2002; Smith 2002). It is the most advanced instrument to observe solar flare emission produced by nonthermal electrons. When operating with both shutters removed, the instrument is able to detect very weak events such as microflares (Benz & Grigis 2002; Krucker et al. 2002). For this study, we select *RHESSI* observations of flare bursts at the shutter-free mode from 2002 May to October. The standard *RHESSI* software (Hurford et al. 2002) is used to retrieve light curves of selected events at a few energy ranges from 3 to 50 keV, which are compared with soft X-ray and microwave observations.

OVSA (Gary & Hurford 1990) is a solar dedicated frequency-agile interferometer, which currently consists of two 27 m antennas and four 2 m antennas. It can observe solar microwave emissions at harmonics of 200 MHz in the range of 1.0–18.0 GHz (up to 86 frequencies) but typically observes at 40 frequencies with a temporal resolution of 8 s. The two large antennas have an rms sensitivity of 0.2 solar flux units (sfu), suitable to detect very weak solar bursts (Gary et al. 1997). The FWHM field of view (FOV) of the large antennas is $46.5/f_{\text{GHz}}$, which is smaller than the solar disk except at the lowest three frequencies. Although the 2 m antennas see the full disk to much higher frequency, their limited sensitivity (~ 5 sfu; Gary et al. 1997) makes them less useful for studies of microflares. Only six events in this study were seen solely by the 2 m antennas. Most of the time during 2002, OVSA observed the active regions that were selected as targets of joint observing campaigns by various instruments in support of *RHESSI*. The microwave observations by OVSA are analyzed using the standard radio calibration software that is developed by the OVSA/New Jersey Institute of Technology group and is built into the Solar SoftWare package (SSW). After the total power calibration and background normalization and subtraction,

microwave bursts with a flux of a few sfu can be unambiguously detected (Gary et al. 1997) when the background emission of the whole Sun is not too strong. In this paper, the microflares observed by OVSA typically have a peak flux of 1–10 sfu.

2.2. Data Selection

In this study, we set some arbitrary criteria to first identify microflares using the *RHESSI* burst catalog and coincident soft X-ray observations by *GOES*. We then identify the selected microflares in microwave observations obtained by OVSA.

A flare catalog can be acquired from the *RHESSI* observing summary data with the starting, peaking, and ending times and the peak count rates of each burst recorded in the photon energy range of 12–25 keV. The shutter status can be also retrieved in the summary data. From 2001 May 1 through October 7, 908 bursts are observed during the open-shutter mode. With these data, we empirically set the criteria for microflare events. An identified *RHESSI* burst is regarded as a microflare if the *RHESSI* peak count rates (in the photon energy range of 12–25 keV) is less than 100 counts s^{-1} and the associated *GOES* soft X-ray incremental flux is below C1.0, or 10^6 W m^{-2} . The *GOES* incremental flux for each individual event is determined by the difference between the maximum and background *GOES* soft X-ray flux at 1–8 Å in the time range from the start to 5 minutes after the end of the *RHESSI* burst. In this way, 760 events are identified as microflares among the 908 bursts. These 760 events are samples for statistical studies and provide a database for case studies. Note that altering the choice of the time range of soft X-rays or lowering the *GOES* incremental flux to the B5.0 level yields only a small change in the number of identified microflares, which does not affect the statistics of the events significantly.

We also compile a catalog of microwave observations by OVSA, which yields 205 *RHESSI* events falling into the OVSA observing window in the time range of 16–23 UT, scattered in 50 days, regardless of whether the events are also identified as microwave bursts by OVSA. Given the work load to analyze all the data, for this first-stage study we have only analyzed microwave data over the 20 days when microflares occur most frequently. During these 20 days, 125 *RHESSI* bursts altogether are found within the OVSA observing window. We calibrate and analyze the hard X-ray and microwave observations during the times of all 125 events and, by inspecting the X-ray and microwave dynamic spectra of each event, determine that 56 of the 125 events are detected in microwaves by OVSA. In Table 1 we list information of the selected 125 events in soft X-ray, hard X-ray, and microwaves.

To illustrate how to identify microwave emissions of *RHESSI* microflares, in Figure 1 we show the hard X-ray and radio dynamic spectra of a microflare that occurred on 2002 July 14. In *GOES* categorization it is a B1.5-class event. The event, which consists of several bursts, is well distinguished in both *RHESSI* and OVSA observations. The microwave dynamic spectrum shown in the figure is observed by one of the two large antennas of OVSA, and its peak flux is below 3 sfu.

The detectability of microflare events in microwaves depends on the field of the view and sensitivity of the OVSA telescopes. Note that of the 56 events that are detected in microwaves, 50 are seen by the two large antennas that usually observe target active regions with a sensitivity down to 0.2 sfu. Only six events are observed solely by the small antennas, which cover a larger FOV but with a lower sensitivity of about 5 sfu (Gary et al. 1997). The 69 events that are not clearly

TABLE 1
LIST OF MICROFLARE SAMPLES

Date	Peaking Time ^a	RHESSI Peak Count Rate ^a	GOES Flux ^b	Radio Signal ^c	OVSA Target AR	
May 1.....	16:34:38	8.0	B6.2/<A	No	AR 9928	
	17:48:18	32.0	B6.5/<A	No	AR 9928	
	19:58:50	30.0	B9.3/B1.6	No	AR 9928	
	22:36:34	12.0	B7.4/A3.7	No	AR 9928	
	22:50:34	13.0	B7.6/A8.9	No	AR 9928	
	23:18:42	8.0	B7.4/A7.3	No	AR 9928	
May 2.....	16:23:26	24.0	C1.1/B1.4	Yes	AR 9934	
	16:34:26	8.0	C1.0/A4.2	Yes	AR 9934	
	16:36:26	11.0	C1.3/B3.2	Yes	AR 9934	
	19:21:10	15.0	B8.3/A8.8	No	AR 9934	
	19:42:18	9.0	B7.8/A5.0	Yes	AR 9934	
	22:53:22	24.0	C3.9/B1.5	Yes	AR 9934	
May 4.....	20:17:30	36.0	B9.9/B1.1	Yes	AR 9934	
	21:26:34	48.0	C1.4/B5.3	Yes	AR 9934	
	23:28:06	10.0	B8.3/A5.1	Yes	AR 9934	
May 6.....	16:37:50	18.0	C1.7/B3.0	No	AR 9934	
	18:06:34	10.0	C1.7/B1.7	Yes	AR 9934	
	22:03:54	100.0	C1.8/B6.4	No	AR 9934	
	23:25:06	9.0	C1.1/A8.9	No	AR 9934	
May 7.....	17:00:30	7.0	B8.7/A3.7	No	AR 9934	
	22:17:54	14.0	B7.5/A4.3	Yes	AR 9934	
May 10.....	17:07:10	18.0	C1.3/B2.1	Yes ^d	AR 9934	
	21:50:54	44.0	C1.1/B3.4	Yes	AR 9934	
	23:44:42	34.0	B9.6/B1.7	Yes	AR 9934	
May 13.....	21:34:30	16.0	C1.2/B1.1	No	AR 9934	
May 27.....	16:10:34	11.0	C1.4/A7.6	No	AR 9957	
	16:36:50	12.0	C1.3/A9.0	No	AR 9957	
	17:13:38	88.0	C2.9/B5.6	Yes	AR 9957	
	17:56:10	24.0	C1.8/B4.4	No	AR 9957	
	20:32:10	48.0	C2.8/B5.3	No	AR 9957	
	20:40:06	14.0	C2.6/B2.3	No	AR 9957	
	20:42:54	24.0	C2.6/B4.6	No	AR 9957	
	20:51:10	10.0	C2.0/A7.6	No	AR 9957	
	22:00:06	9.0	C1.2/B2.9	Yes	AR 9987	
	Jun 10.....	19:02:18	68.0	C1.3/B3.6	Yes	AR 8
		20:23:22	10.0	C1.0/B1.0	Yes	AR 19
21:12:30		52.0	C1.5/B6.9	No	AR 19	
Jul 14.....	22:12:50	52.0	B9.7/B3.1	No	AR 19	
	16:23:58	52.0	B7.7/B1.5	Yes	AR 30	
	17:42:02	10.0	C1.1/A9.4	Yes	AR 30	
	19:00:26	12.0	B7.9/A5.6	Yes	AR 30	
	20:42:10	9.0	B6.3/A2.8	No	AR 30	
	22:00:38	22.0	B8.7/B1.7	Yes	AR 30	
	22:12:42	9.0	B6.7/A1.7	Yes	AR 30	
	23:32:54	15.0	C1.7/B5.4	No	AR 30	
Jul 15.....	16:35:30	16.0	B9.3/A6.6	No	AR 30	
	17:17:54	44.0	C1.4/B2.3	Yes	AR 30	
	18:01:54	20.0	C1.7/B2.1	Yes	AR 30	
	18:05:06	16.0	C1.7/A7.6	Yes	AR 30	
	19:12:42	30.0	C1.3/B2.9	No	AR 30	
	19:31:22	16.0	C1.1/A2.2	No	AR 30	
	23:52:46	36.0	C3.7/B3.1	No	AR 30	
	Jul 26.....	16:35:26	7.0	C2.3/B2.2	No	AR 39
16:47:42		34.0	C2.1/A8.7	No	AR 39	
16:58:54		40.0	C2.4/B4.4	Yes	AR 39	
17:15:10		11.0	C2.0/B1.5	Yes	AR 39	
17:26:34		60.0	C2.0/B2.4	Yes	AR 39	
20:14:42		18.0	C2.6/B1.8	Yes	AR 39	

TABLE 1—Continued

Date	Peaking Time ^a	RHESSI Peak Count Rate ^a	GOES Flux ^b	Radio Signal ^c	OVSA Target AR	
Aug 10	16:21:18	16.0	C1.4/<A	No	AR 61	
	16:43:34	64.0	C2.2/B4.5	Yes	AR 61	
	18:05:26	26.0	C1.2/B1.1	No	AR 61	
	18:27:06	11.0	B9.9/A3.6	No	AR 61	
	19:35:42	30.0	C1.1/B1.9	Yes	AR 61	
	19:53:54	18.0	C1.0/A3.7	No	AR 61	
	19:56:46	10.0	B9.9/A3.8	No	AR 61	
	20:08:06	34.0	C1.4/B4.7	No	AR 61	
	21:10:18	10.0	C1.1/B1.1	No	AR 61	
	21:26:50	18.0	B8.9/A3.6	Yes	AR 61	
	21:34:42	26.0	C1.3/B2.2	Yes	AR 61	
	21:54:18	9.0	B8.8/A4.4	No	AR 61	
	22:47:26	9.0	C1.1/B1.1	No	AR 61	
	23:20:10	15.0	C1.3/B2.2	No	AR 61	
	23:27:02	12.0	C1.4/B1.7	Yes	AR 61	
23:36:10	84.0	C1.7/B6.2	No	AR 61		
Aug 12	16:58:14	10.0	C1.1/A7.8	Yes	AR 69	
	17:06:54	10.0	C1.3/A5.7	Yes	AR 69	
	18:31:26	28.0	C2.2/B6.1	Yes	AR 69	
	19:59:10	92.0	C2.6/B6.8	Yes ^d	AR 69	
	20:19:34	16.0	C1.9/A7.6	Yes	AR 69	
Aug 14	21:30:54	46.0	C1.3/B2.7	Yes	AR 69	
	17:12:22	52.0	C1.4/B3.2	Yes	AR 69	
Aug 17	16:56:58	14.0	C2.1/B1.5	No	AR 69	
	18:41:18	64.0	C2.0/B5.7	Yes	AR 69	
	18:46:34	32.0	C2.0/B4.1	No	AR 69	
	19:06:22	72.0	C1.6/B2.3	Yes	AR 69	
	20:13:46	18.0	C2.3/B3.8	Yes	AR 69	
	20:19:22	13.0	C2.0/B1.6	Yes	AR 69	
	20:23:38	13.0	C1.8/B2.3	No	AR 69	
	22:03:26	9.0	C1.2/A4.0	Yes	AR 69	
	23:23:30	16.0	C2.0/B2.3	No	AR 69	
	23:34:42	13.0	C1.7/A7.6	Yes	AR 69	
	23:46:26	52.0	C1.7/B1.5	Yes	AR 69	
	Aug 19	18:42:50	9.0	C2.2/<A	No	AR 69
		18:45:30	14.0	C2.2/A7.6	No	AR 69
		18:46:58	26.0	C2.2/B1.5	Yes ^d	AR 69
		19:14:02	24.0	C1.8/A7.6	Yes	AR 69
19:16:42		11.0	C1.8/B1.5	No	AR 69	
19:18:34		24.0	C1.8/B2.2	Yes	AR 69	
20:32:34		52.0	C1.7/A7.6	No	AR 69	
20:34:58		16.0	C2.4/B7.3	Yes	AR 69	
22:21:14		72.0	C4.1/B3.0	No	AR 69	
19:22:54		3.0	B7.6/A1.1	No	AR 119	
19:31:46		6.0	B7.8/A1.4	No	AR 119	
20:30:26		76.0	C1.4/B5.9	Yes	AR 119	
20:59:26		4.0	B5.3/A2.9	No	AR 119	
Sep 24		21:09:22	7.0	B5.2/A2.9	No	AR 119
		21:57:06	4.0	B5.1/<A	Yes ^d	AR 119
	22:08:02	36.0	B6.1/A9.1	No	AR 119	
	22:11:30	6.0	B6.0/A7.3	No	AR 119	
	22:35:34	4.0	B5.6/A4.8	No	AR 119	
	22:40:46	10.0	B6.1/A8.8	No	AR 119	
	22:48:18	9.0	B6.9/B1.1	No	AR 119	
Sep 26	19:06:38	7.0	B9.0/B1.4	Yes ^d	AR 132	
	19:10:46	17.0	C1.1/B2.9	Yes ^d	AR 132	
	20:37:30	12.0	C1.2/B5.7	No	AR 132	
	22:02:26	6.0	B7.4/A6.5	No	AR 132	
	22:29:38	10.0	B7.6/A8.9	No	AR 132	

TABLE 1—Continued

Date	Peaking Time ^a	<i>RHESSI</i> Peak Count Rate ^a	<i>GOES</i> Flux ^b	Radio Signal ^c	OVSA Target AR
Sep 29	17:46:30	9.0	B5.0/A3.6	No	AR 134
	18:02:46	4.0	B5.2/<A	No	AR 134
	18:11:42	10.0	B5.5/A1.7	No	AR 134
	19:49:30	7.0	B5.2/A2.9	No	AR 134
	21:29:50	14.0	B9.7/B3.3	No	AR 134
	22:34:30	9.0	C1.5/B2.3	No	AR 134
	22:52:58	56.0	C2.2/B9.8	No	AR 134
	23:12:30	8.0	C1.1/A9.3	No	AR 134

NOTE.—Total number of events $N_{\text{tot}} = 125$.

^a From the *RHESSI* flare catalog in the 12–25 keV photon energy range.

^b *GOES* absolute and incremental flux at 1–8 Å.

^c “Yes” indicates that the event was identified by OVSA telescopes.

^d Events detected only by small antennas.

identified in microwaves may mostly occur outside the field of view of the large antennas. Figure 2a shows the peak frequency distribution of 50 events seen in microwaves by large antennas. About 90% of these events peak at ≥ 4 GHz, and the average peak frequency is 6.6 GHz. These statistics agree well with the peak frequency for all events seen with OVSA over 2 yr of observations (Nita et al. 2004). At 6.6 and 4 GHz, the beam FWHM of the OVSA large antennas is roughly 7' and 12', respectively, yielding a coverage of 6%–15% of the solar disk area. The fact that over 40% of *RHESSI* microflares are detected in microwaves strongly suggests that microflares are not evenly distributed across the solar disk, but rather a large percentage of *RHESSI* microflares occur in active regions that are observed by OVSA.

The locations of many events can be retrieved from the *RHESSI* summary data, which can be compared with the OVSA pointing. In Figure 2b we plot the difference between

the flare location and OVSA pointing for 33 events that are observed by both *RHESSI* and the OVSA 27 m antennas. The figure shows that for most events, the difference between the *RHESSI* location and OVSA pointing is within 200". Among the five events that show a large difference, three are observed by OVSA only at very low frequencies below 5 GHz, where the FOV of the antennas is relatively large. In the other two events, multiple sources at different locations are found in the disk simultaneously. Figure 2b confirms that the majority of microflares observed by both instruments occur in the OVSA targeted active regions. These results in Figure 2 indicate that OVSA is able to detect most hard X-ray microflares seen by *RHESSI* in the 12–25 keV range.

3. CHARACTERISTICS OF MICROFLARES

We examine the general characteristics, including flux distribution and magnitude, of the identified microflare events

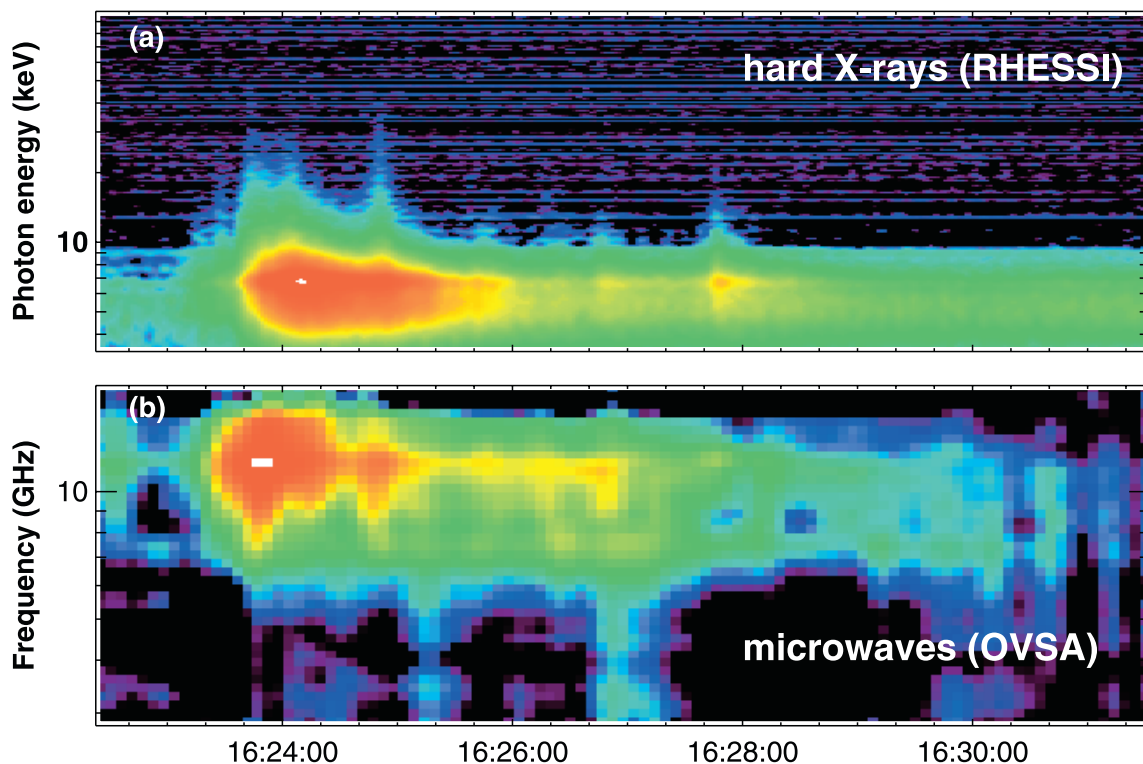


FIG. 1.—Dynamic spectra of (a) *RHESSI* hard X-ray and (b) OVSA microwave total power of a B1.5 event observed at 16:23 UT on 2002 July 14.

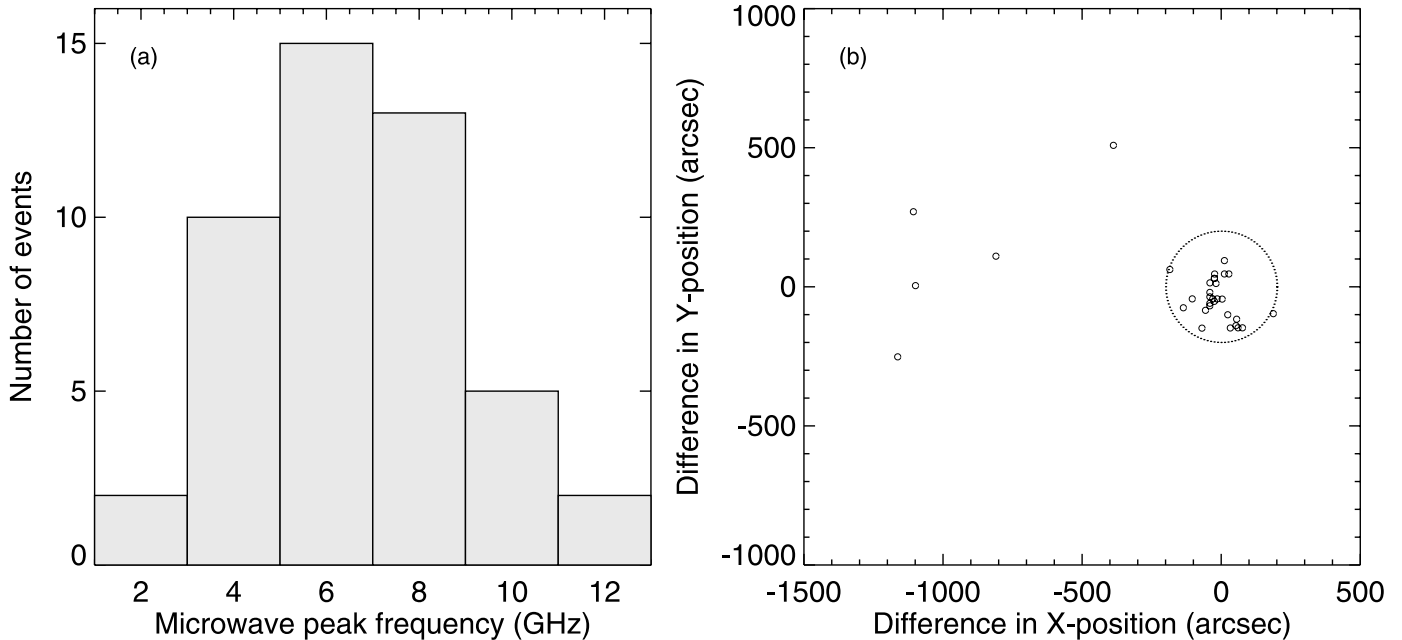


FIG. 2.—(a) Peak frequency distribution of microflares observed by OVSA large antennas. (b) Difference between OVSA 27 m antenna pointing and X-ray source location from *RHESSI* observing summary for 33 events that are observed by both *RHESSI* and OVSA large antennas. The circle indicates a position difference of $200''$.

and then investigate the relationship between microflare occurrence and solar activity by studying the temporal and spatial distribution of microflares. These properties are also compared with those of large flares.

3.1. Flux Distribution

Figure 3 shows the scatter plot of the *RHESSI* peak count rates against the *GOES* flux of the events studied in this paper. It is seen that, in general, *RHESSI* peak count rates are positively correlated with *GOES* flux, and the identified microflares that have small flux in soft X-rays are usually also weak in hard X-rays.

Figure 3b shows the scatter plot of the *RHESSI* peak count rates against the microwave peak flux of the 50 microflares that are observed by OVSA large antennas. The two are also roughly scaled, the cross-correlation coefficient being 0.16 with a 70% confidence level. The peak flux of microwaves falls between 1 and 10 for most of the events. It should be noted that a large number of smaller events with a flux level of less than 2 sfu might not be present in this plot as a result of our selecting *RHESSI* microflares in the energy range of 12–25 keV. This point will be further discussed in the following text.

To display the statistical properties of the events, in Figure 4 we plot the event number distributions with respect to *GOES* peak flux and *RHESSI* peak count rates for all (908) events observed during the open-shutter mode, the identified microflare events (760), and the sample events (125) jointly observed by both *RHESSI* and OVSA. The figure suggests a power-law distribution of the events as a function of the soft X-ray peak flux and hard X-ray peak count rates. The power-law distribution $dN/dF \sim F^{-\alpha}$ is best achieved by using the *RHESSI* peak count rates, which yields a power-law index $\alpha = 1.75 \pm 0.03$. With the background subtracted, there is a very slight change in the distribution with $\alpha = 1.73 \pm 0.03$. We note that emissions in the 12–25 keV energy range can contain both thermal and nonthermal contributions. To compare with

previous results from numerous other studies using hard X-ray and radio data by different instruments (Crosby et al. 1993; Nita et al. 2001 and references therein), detailed spectral analysis is necessary to obtain the frequency distribution of the nonthermal flux rather than uncalibrated count rates. It is also noteworthy that pulse pileup may affect the frequency distribution even down to peak count rates of 10 counts s^{-1} (Rauscher et al. 2003). Since large events are more affected, the real distribution is expected to be steeper than shown in Figure 4c.

The power-law fits to the frequency distributions versus soft X-ray absolute and incremental peak flux yield a logarithmic slope of 2.32 ± 0.19 and 1.60 ± 0.07 , respectively. The first number is consistent with Veronig et al. (2002), who derived $\alpha = 2.11 \pm 0.13$ using 1–8 Å *GOES* soft X-ray peak flux of 49,409 events from 1976 to 2000 without background subtraction. With the background subtracted, the power-law shape of the 908 events in this paper is much flattened, but the derived α is still smaller than previously reported values of 1.86 by Lee et al. (1995) and 1.88 by Feldman et al. (1997) using *GOES* soft X-ray data with background subtracted. The reason for the flatter frequency spectrum shown in Figure 4b may lie in our choice of the background within a relatively short time range, namely, from the start to 5 minutes after the end of *RHESSI* burst.

The rollover of the frequency distribution shown in Figure 4 is usually believed to be a result of limitations in instrument sensitivity or burst identification algorithm rather than a low-flux cutoff of physical significance. Despite a much smaller number of events studied in this paper in comparison with Veronig et al. (2002), the rollover at $(1-2) \times 10^{-6} \text{ W m}^{-2}$ shown in Figure 4a is about the same as in Veronig et al. (2002). However, the flux distribution in Veronig et al. (2002) is less steep in the low-flux range below the rollover than that of the 908 events that have *RHESSI* hard X-ray counterparts in 12–25 keV. This result is an indication that many soft X-ray events in the low-flux range may not have perceivable hard

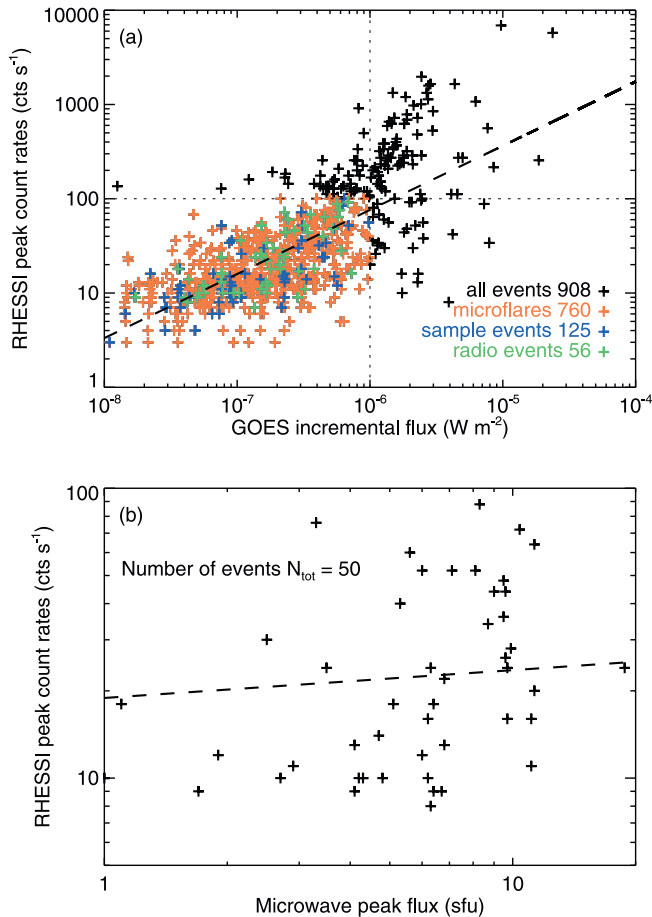


FIG. 3.—Scatter plot of the peak count rates of *RHESSI* bursts in 12–25 keV against (a) *GOES* soft X-ray incremental flux and (b) microwave peak flux observed by OVSA large antennas (see text). In (a), the dashed line is a least-squares linear fit to all 908 events, and the dotted lines indicate the thresholds in *RHESSI* peak count rates and soft X-ray flux to select microflares. In (b), the dashed line shows a least-squares linear fit to the data. The correlation coefficient is 16% with a 70% confidence level.

X-ray counterparts beyond 12 keV. In Figure 4c, the rollover at around 8 counts s^{-1} may indicate the sensitivity limit of *RHESSI* in the 12–25 keV energy range, or it may be that the *RHESSI* software fails to recognize many weaker events when generating the burst catalog used in this study.

In Table 2, we list the mean soft X-ray incremental flux and *RHESSI* peak count rates of the 760/125/56 events as an

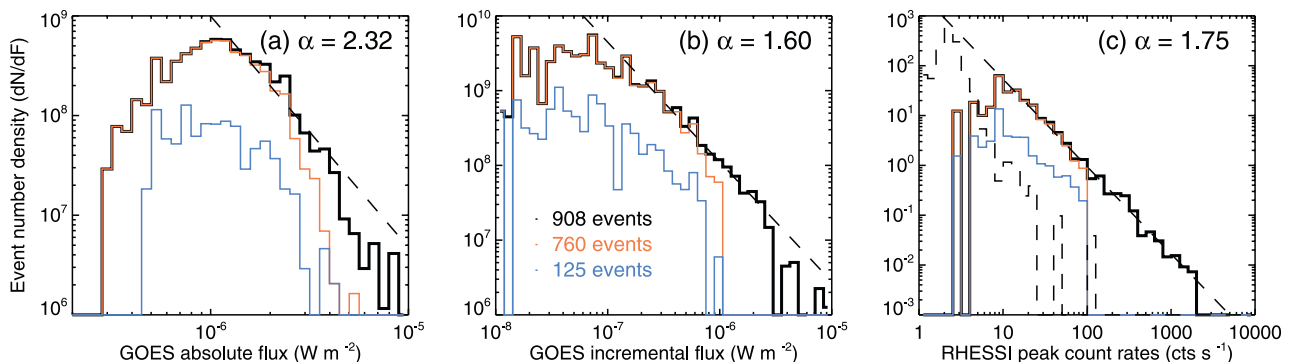


FIG. 4.—Frequency distribution of *GOES* 1–8 Å soft X-ray (a) absolute flux, (b) incremental flux, and (c) *RHESSI* peak count rates. The dark dashed histogram in (c) shows the distribution of *RHESSI* background count rates. The quantity α is the logarithmic slope of the fit to all events (dashed line) above the rollover point, namely, C1, B1, and 9 counts s^{-1} for (a), (b), and (c), respectively.

indication of the magnitude of the selected populations of events. For all three populations, the events are, on average, of B2 class in *GOES* categorization, and the mean *RHESSI* peak count rate is around 20 counts s^{-1} in the 12–25 keV photon energy. Specifically, the mean flux level of the 56 events, of which corresponding microwave bursts are detected, is not significantly higher than the average population, suggesting that among the samples under our consideration the “visibility” of these events in microwaves is not subject to the X-ray magnitude of the events.

The results shown in Figures 3 and 4 and Table 2 also suggest that the 125 sample events and the 56 microwave events are rather evenly scattered among all 760 microflares, and their frequency distributions exhibit nearly the same logarithmic slope as that of the total events. Therefore, selection of these 125/56 events as samples for further studies is unlikely to lead to a biased conclusion from a statistical point of view.

3.2. Occurrence Rate

To illustrate the temporal distribution of microflares with respect to solar activity, in Figure 5 we plot the *GOES* flux in 1–8 Å from 2002 May 1 through September 30 with the peak count rates of over 700 *RHESSI* microflares superposed. The time range of the *RHESSI* open-shutter mode is indicated by gray shading. If we look at the monthly distribution, the figure shows that when the solar activity is relatively low, as indicated by the relatively low soft X-ray flux level, there are fewer *RHESSI* microflares as well. The month of 2002 June is a typical example showing that when the *GOES* soft X-ray level is below C level most of the time, the number of events is much smaller than in other months by a factor of 4–6. This figure alone shows qualitatively that the rate of microflare events considered in the current study is correlated with solar activity as represented by the soft X-ray total flux recorded by *GOES*.

More quantitatively, we can estimate the event occurrence rate in terms of number of events per hour. Since the observation coverage is not uniform, we only estimate the monthly mean of the event rate R_m as shown in Figure 6. To derive R_m , we count the total number of microflares for each month and then divide it by the total hours when *RHESSI* was observing in open-shutter mode. In the estimation, the durations of satellite night, South Atlantic Anomaly transition, and data gaps are taken into account. Figure 6 shows that R_m is on the order of 0.2–5 hr^{-1} , with the minimum in June.

The occurrence rate of microflares is also compared with that of large events. The dashed lines in Figure 6 show the

TABLE 2
MAGNITUDE OF MICROFLARES

Population	Total Number	GOES Incremental Flux ^a	RHESSI Peak Count Rates ^{a,b}
All microflares	760	B2.1 ± B2.0 (B1.5)	23 ± 18 (16)
Sample.....	125	B2.0 ± B1.9 (B1.4)	24 ± 21 (15)
Radio.....	56	B2.2 ± B1.8 (B1.7)	27 ± 22 (18)

^a The mean (median) value of the flux.
^b Refers to the 12–25 keV energy range.

monthly averaged occurrence rate of events at all scales that are recorded by *RHESSI* during the same period regardless of shutter status. It is shown that the occurrence rate of the microflares in general follows the rate of large flares, and both exhibit a minimum in June, which is lower than the rate in other months by 0.5–1 order of magnitude. The big difference between the rate of microflares and large flares in September might be caused by the fact that the duration of shutter-free mode in this month is too short (Fig. 5) to yield results that are statistically comparable with other months.

We note that the derived R_m shown in Figure 6 is lower than quoted values in the literature by 1 order of magnitude (Lin et al. 1984; Shimizu 1995; Benz & Grigis 2002). We consider that the major reason for such a discrepancy is that

microflares in this study are selected from a *RHESSI* burst catalog compiled in the 12–25 keV energy range, which might not include many smaller events, as suggested by the steep peak flux/count spectra below the rollover (Fig. 4) and, as well, the lack of weak (<2 sfu) microwave events (Fig. 2b). In a simple-minded way, if we extrapolate the *RHESSI* peak count rate distribution to a sensitivity that is nominally raised to 1 count s⁻¹ in 12–25 keV, given the power-law index $\alpha = 1.75$, the total number of events will increase fivefold. The smaller events should be seen in lower energy ranges than 12–25 keV. Benz & Grigis (2002) visually inspected *RHESSI* observations from 3 to 12 keV during a selected observing time of 373 minutes and determined the event occurrence rate to be 10.3 hr⁻¹. Most events in their study do not have perceivable

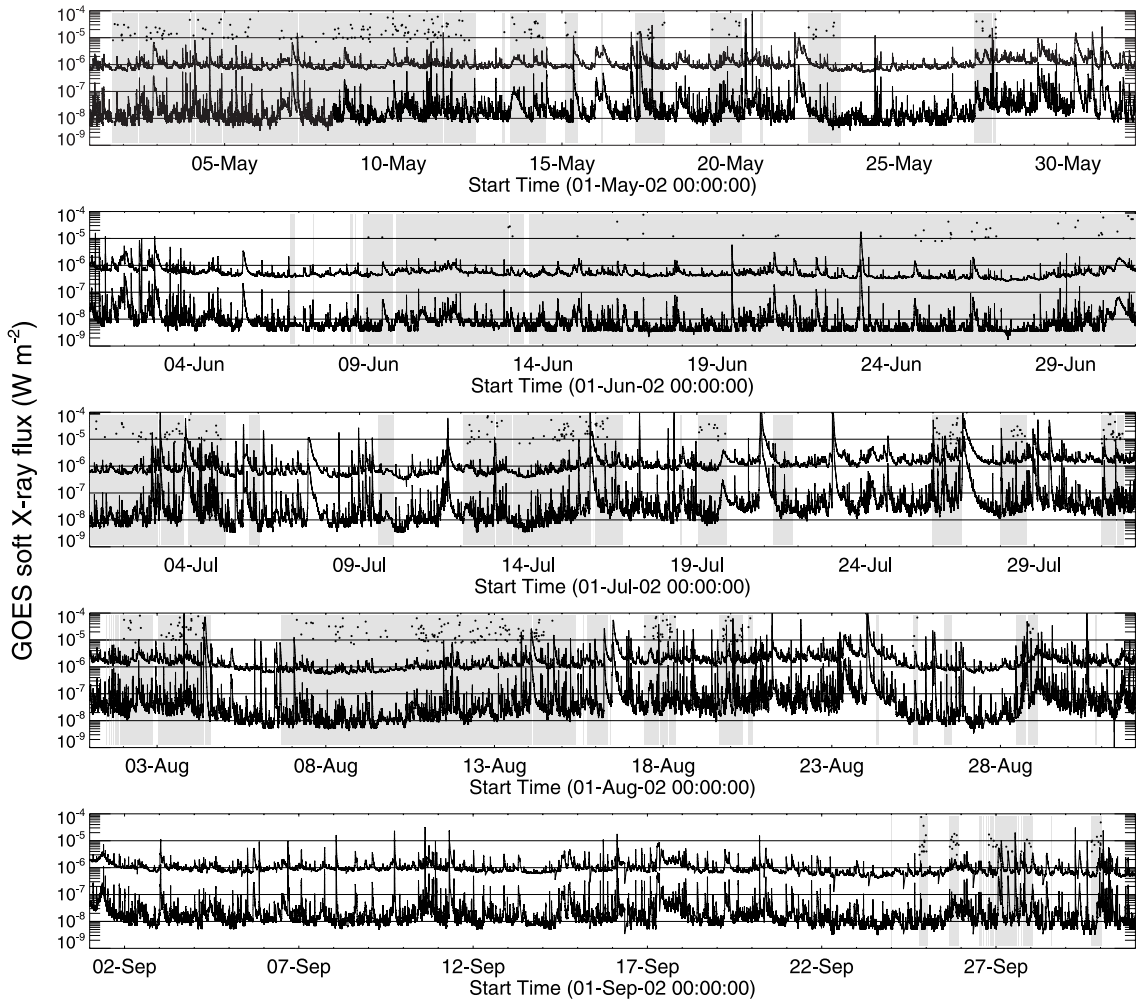


FIG. 5.—Distribution of *RHESSI* microflares with respect to solar activity. The curves show the time profiles of *GOES* 1–8 Å and 0.5–4 Å soft X-ray flux from 2002 May 1 through September 30, superposed with the peak count rates, in units of 10⁶ counts s⁻¹, of over 700 *RHESSI* microflares (dark dots). The shaded areas indicate the time ranges when *RHESSI* operates in open-shutter mode.

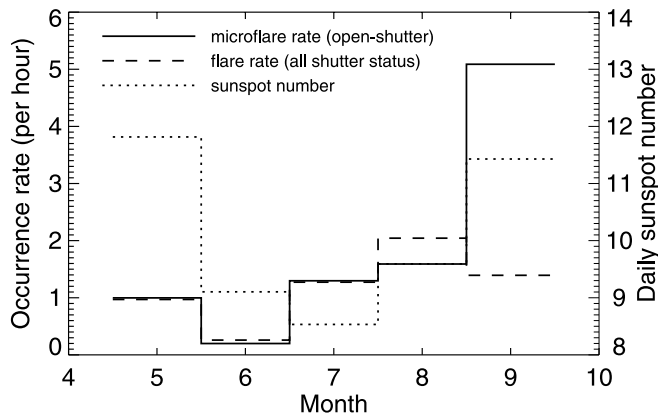


FIG. 6.—Monthly averaged occurrence rate of microflares (solid line) observed during *RHESSI* open-shutter mode and flares of all sizes (dashed line) detected regardless of the shutter status from 2002 May through September, superposed with the monthly mean of daily sunspot number (dotted line) counted by Mount Wilson Observatory.

emission beyond 12 keV, so it is not clear how many microflares in their study are primarily heating events with negligible nonthermal content. Comparison with the result of Benz & Grigis (2002) requires knowledge of the photon spectral properties, including the thermal and nonthermal characteristics of the events, nonthermal spectral index, and lower energy/flux cutoff, without which estimates of the event occurrence rate will be rather arbitrary and can easily vary by orders of magnitude.

3.3. Active Region Distribution

Stemming from Figures 5 and 6, the next question to ask is what determines the temporal distribution of the flare bursts at all scales. We expect that the answer will be related to variations in the complexity of magnetic fields. The effort to map and locate the identified microflares in the magnetograms is beyond the scope of this work. In our first-stage study, we provide some alternative means that can shed some light on this issue. A simplest way is to examine whether the number of microflares is correlated with the number of active regions or sunspots. We take the daily sunspot number counted by Mount Wilson observatory³ from May to September and in Figure 6 plot the monthly mean of the daily sunspot number in comparison with the monthly mean of the microflare event rate. It is shown that the number of sunspots reaches a minimum in July, although the minimum of the microflare rate occurs in June. The plot therefore suggests that the microflare event rate is not entirely correlated with the number of sunspots on the monthly timescale. In other words, either a significant number of microflares do not occur in active regions, or active regions, as determined from sunspot numbers, are not equally productive in microflares.

Another clue to the location of microflares can be obtained by exploring microwave observations. Figure 2 suggests that indeed a large number of microflares occur in the target active regions that are usually expected to produce large solar flares. As an example, Figure 6 shows three active regions that are found to be most productive in microflares in May (Fig. 7a), July (Fig. 7b), and August (Fig. 7c). Judged from whether the microflares are detected by the OVSA big antennas and from

the limited number of *RHESSI* quick-look images, we find that about $\frac{2}{3}$ microflares occur in the above three active regions during their disk transit. Therefore, as in the case of large flares, certain active regions are a lot more productive in microflares than other active regions.

We remind the readers that in this study microflares registered in the 12–25 keV range are most probably nonthermal in character. Using *Yohkoh* observations, Nitta (1997) found that almost all soft X-ray microflares that have hard X-ray counterparts were located in a large and complex active region with strong magnetic fields, while those events without perceivable hard X-rays occurred in other regions. Such observations suggest that if we search lower energy ranges, e.g., down to 3 keV, for microflares, it is possible that more microflares can be located in different active regions from the ones that dominantly produce 12–25 keV microflares.

Looking at Figure 7, it is not difficult to understand why these three regions are the most productive. Each of the three regions occupies the greatest area and exhibits the most complex magnetic structure compared with other regions on the solar disk during the same periods (e.g., Fig. 7c). All three active regions develop into $\beta\gamma\delta$ structures when they mature. The active regions NOAA 30 and NOAA 69 that dominate during July and August, respectively, produce both microflares and very large flares. Counted from the *GOES* solar X-ray events catalog, during July 10–23, 56/8/3 flares of C/M/X class are produced in NOAA 30 compared with 42/2/1 from all other regions, and during August 13–25, 98/30/4 flares of C/M/X class are produced in NOAA 69 compared with 82/16/0 in all other regions. Such a result suggests that some large and complex active regions are prone to producing flares of all sizes.

On the other hand, during the first half of May, the active region NOAA 9934 where most microflares take place does not produce very large flares. For most of the events in 2002 May, first-look maps are provided at the *RHESSI* Web site. In the next section, we study, in more detail, the spatial distribution of these events and the productivity of active regions.

3.4. Productivity of AR 9934

In the first half of May, we find 24 microflare events from May 1 to 13 from our list of 125 events. These are relatively weak events with average *GOES* incremental flux at the B1.0 level. Most interestingly, we find that 16 of the 24 microflares are located in the same active region NOAA 9344 on the basis of the quick-look maps provided by P. Saint-Hilaire at the *RHESSI* Web site.⁴ The remaining eight events either cannot be mapped or occur in other active regions. Therefore, at least $\frac{2}{3}$ of microflares from May 1 through May 13 are produced by the active region NOAA 9934, although during the same period there are over 10 active regions in the solar disk each day (Fig. 7a).

It is suggestive to compare NOAA 9934 with other regions in terms of their productivity of flares at varying scales. An online catalog of *GOES* X-ray events is compiled by P. T. Gallagher⁵ with the location and magnitude (measured by the incremental soft X-ray flux at 1–8 Å) of each event corrected from the NOAA flare list (P. T. Gallagher 2003, private communication). Using this catalog, we plot in Figure 8 (top) the number of flares, which are usually of larger scales than the identified microflares, in each active region from May 1 to 13. The figure

³ See <http://www.astro.ucla.edu/%7Eobs/spotframe.html>.

⁴ See http://www.hedc.ethz.ch/www/quick_dp_search.html.

⁵ See <http://beauty.nascom.nasa.gov/arm/latest>.

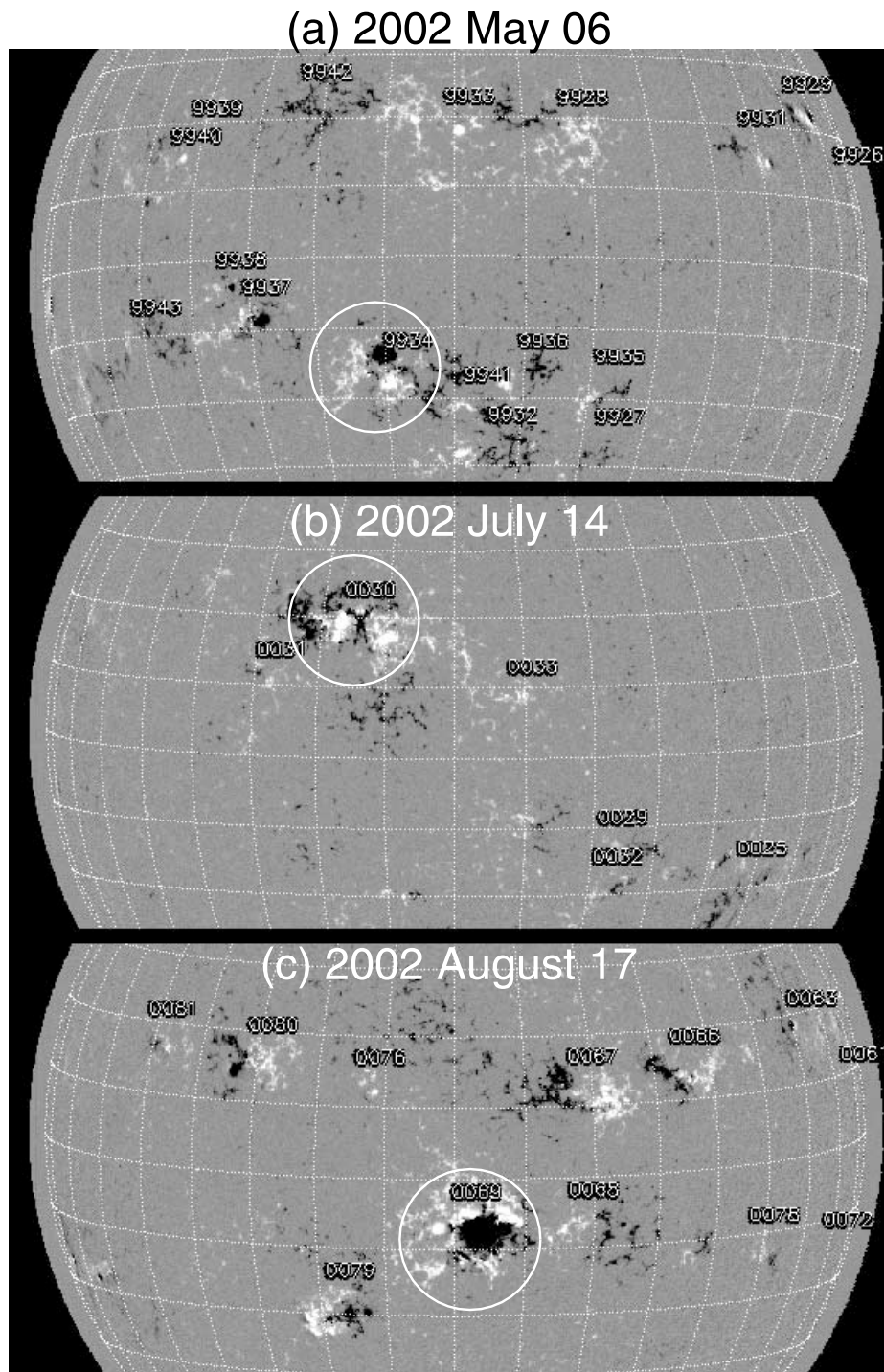


FIG. 7.—Snapshot of the Sun's longitudinal magnetogram in (a) 2002 May, (b) 2002 July, and (c) 2002 August. The white circles indicate active regions that are found to be most productive of *RHESSI* microflares.

shows that, unsurprisingly, the number of events are not evenly distributed over all active regions, but some active regions are more inclined to produce events than others. As in the case of microflares, the majority of larger flare events are also produced in NOAA 9934 during the first half of May; i.e., the active region NOAA 9934 is very productive compared with other active regions during the same period of time. The large number of flares counted in NOAA 9934 may be partly due to the fact that the region is observed throughout its disk transit, but this fact alone does not lead to the great contrast against other

active regions; note that the second most productive region NOAA 9937 produces less than one-half the events produced in NOAA 9934.

However, NOAA 9934 does not produce very big solar events compared with other regions. As shown in Figure 8 (*bottom*), the mean flux level of NOAA 9934 events is not very high. On average, the magnitude of the events in NOAA 9934 is less than C2.7, and the largest event ever produced during its disk transit is a C7.8 event, while all the M-class events during this half-month are produced in other regions. This result shows that in the case

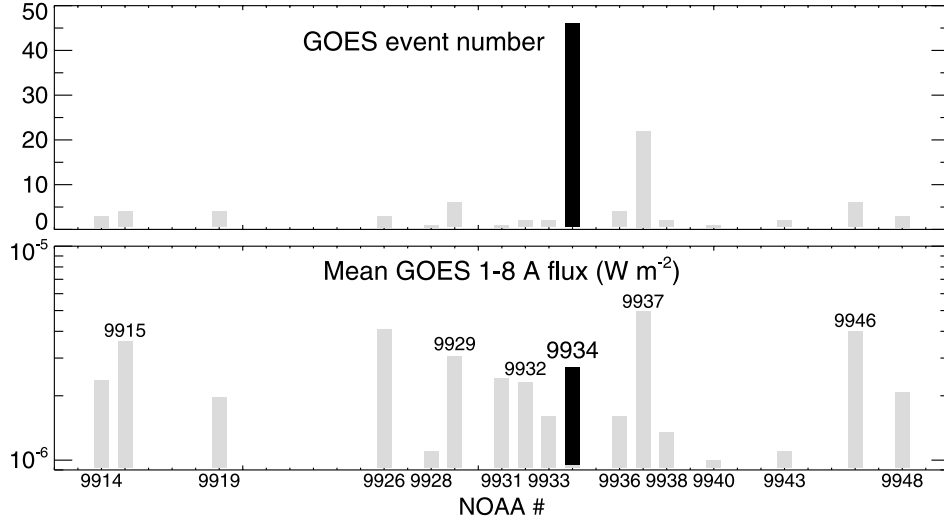


FIG. 8.—*Top*, Number distribution, and *bottom*, mean 1–8 Å soft X-ray flux of *GOES* flares in different active regions on the Sun’s disk from 2002 May 1 through 13. The dark bars denote the active region NOAA 9934 that is most productive of microflares.

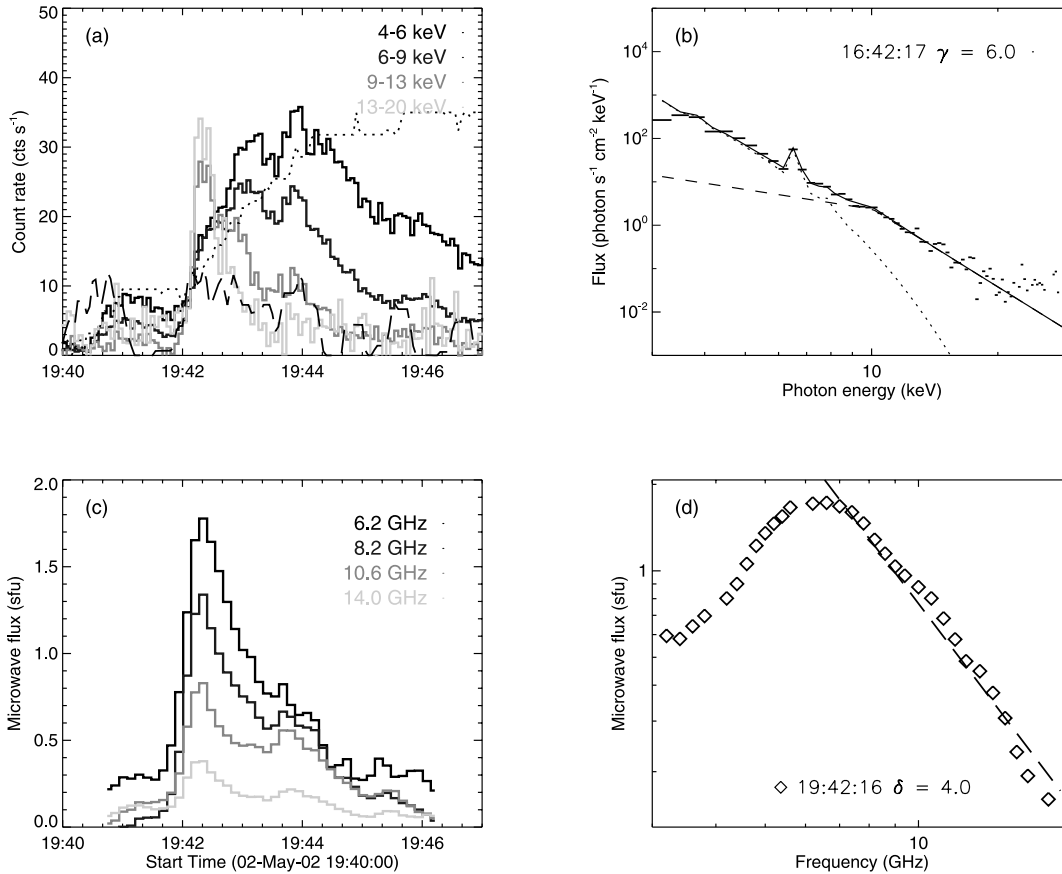


FIG. 9.—X-ray and microwave light curves and spectra for the microflare at 19:42 UT on 2002 May 2. (a) Time profiles of *RHESSI* burst count rates in different energies. The scale of the y -axis indicates the peak count rates of the hard X-rays in the lowest energy, and light curves at other energies are normalized to arbitrary units. The dotted and dashed lines indicate *GOES* 1–8 Å soft X-ray emission and its time derivative, both normalized to arbitrary units. (b) *RHESSI* photon flux spectrum (*short horizontal bars*) and its best fit (*dark solid line*; see text) at given times. The dotted and dashed lines show the thermal and power-law components, respectively, from the fit; γ is the power-law slope from the fit. (c) Microwave total power flux at varying frequencies observed by one of the two *OVSA* large antennas. (d) Microwave total power spectrum (*symbols*) and the fit (*dashed line*; see text) to its optically thin part at given times; δ is the electron power-law index derived from the fit and the approximation formula by Dulk & Marsh (1982).

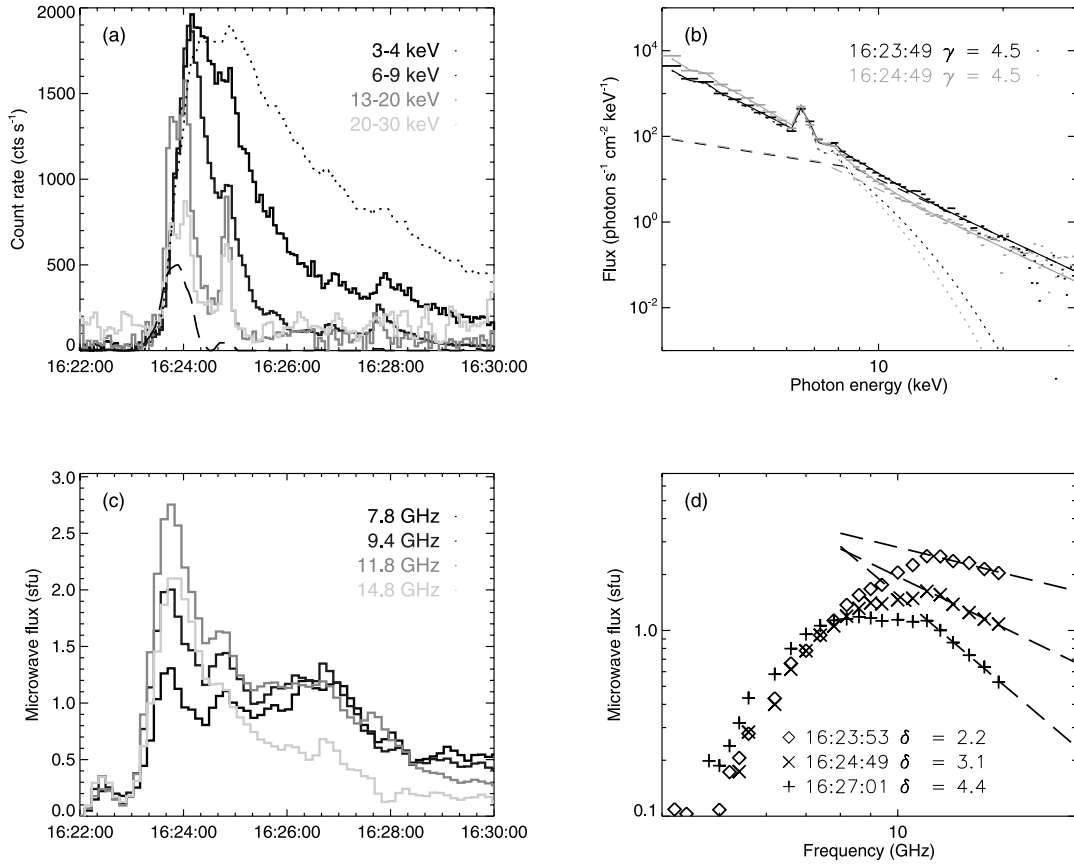


FIG. 10.—Same as Fig. 9, but for the microflare at 16:23 UT on 2002 July 14.

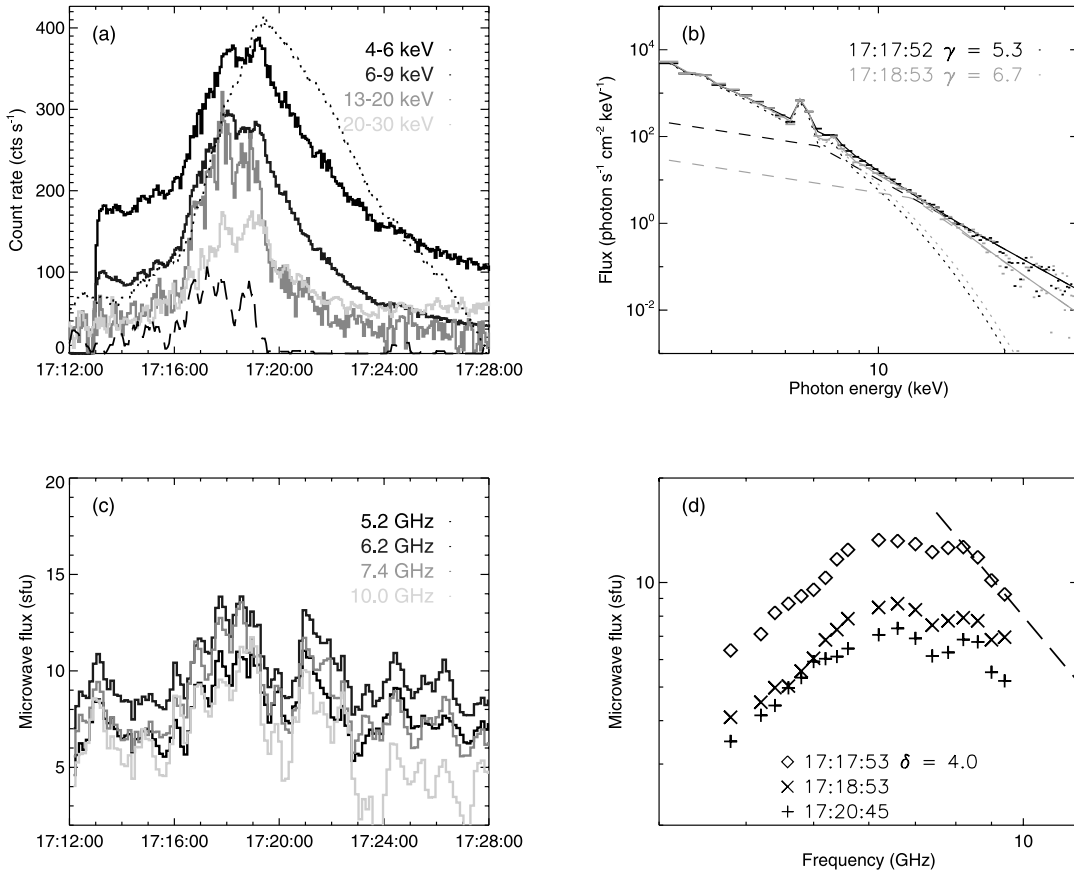


FIG. 11.—Same as Fig. 9, but for the microflare at 17:17 UT on 2002 July 15.

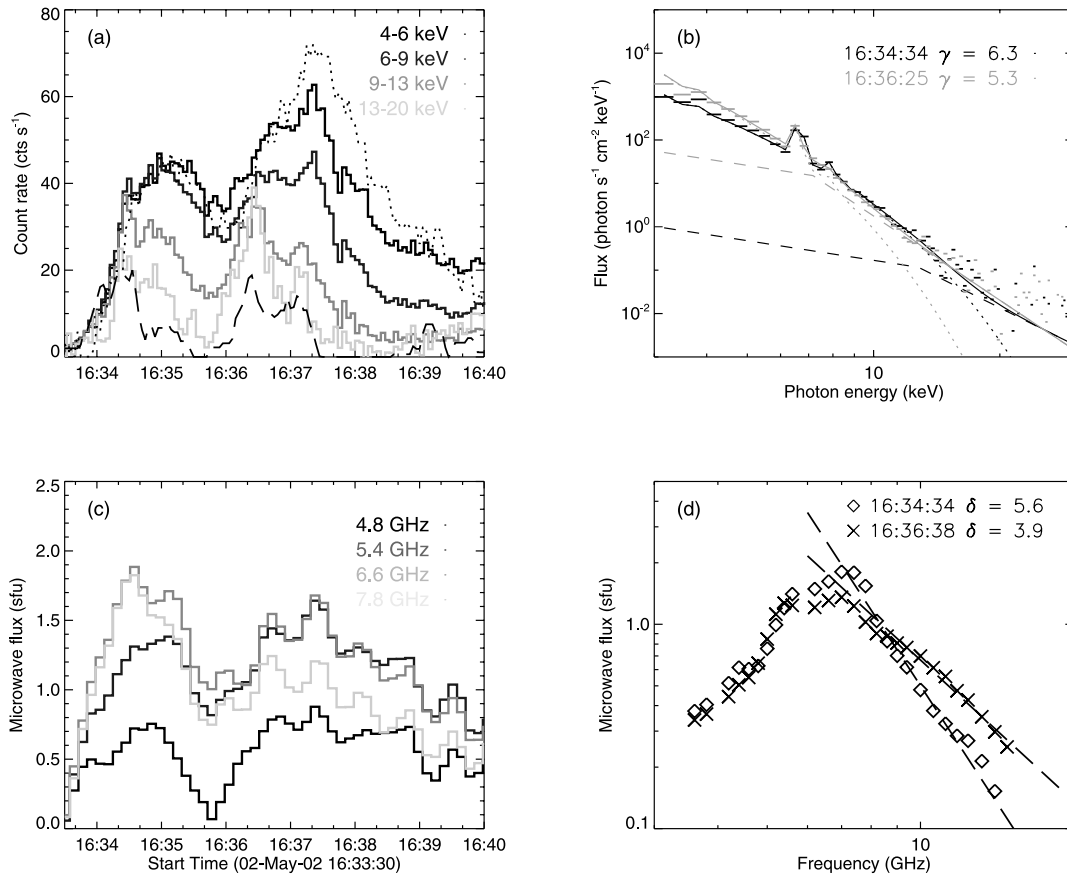


FIG. 12.—Same as Fig. 9, but for microflares at 16:34 and 16:36 UT on 2002 May 2.

of NOAA 9934, small flares or microflares are not precursors of very large events. It will be important to understand why NOAA 9934 behaves differently from NOAA 30 and NOAA 69 in terms of the flare productivity. It may be related to the properties of active regions and their evolution (e.g., Kucera et al. 1997; Nitta 1997), which is beyond the scope of this paper.

4. NONTHERMAL SIGNATURES OF MICROFLARES

Most of the analyzed microflares are observed by *RHESSI* at energies of over 10 keV, and the microwave emission of many events can be detected at around 10 GHz. These are indications of nonthermal signatures of microflares. To study the details of X-ray and microwave emissions in microflares, in Figures 9–12, we demonstrate the time and spectral profiles of some events observed in X-rays and microwaves. The X-ray light curves obtained from *RHESSI* are semicalibrated count rates of photons (counts per second) received by all nine detectors and integrated in a few energy ranges over 4 s. In the plots all the light curves are background subtracted.

4.1. Energy-dependent Time Profiles

Figures 9–12 show that the light curves of most analyzed events are characterized by a fast rise and a slow decay. Usually emissions at higher energies of above 10 keV rise impulsively and reach maximum ahead of emissions at lower energies, such as less than 10 keV X-rays observed by *RHESSI* and *GOES*. We measure the time lags of *RHESSI* hard X-ray emissions with respect to emission at 6–9 keV using a cross-correlation approach and plot in Figure 13a the average time lags of more than 100 events. On average, emission at 3–4 keV is delayed by about 5 s with respect to emission at 14–20 keV.

In most events, emission beyond 20 keV is at noise level; hence, no reliable time lag analysis can be performed. We also measure the time lags of microwaves with respect to hard X-rays in 12–25 keV and plot in Figure 13b the time lag distribution of 50 events observed in both wavelengths. The results show that microwave light curves are correlated with greater than 10 keV hard X-rays, and within the temporal resolutions of the two instruments, greater than 10 keV hard X-rays and microwaves reach the maxima simultaneously in the early phase of the flare in most events. Figures 9–12 also show that microwave bursts usually exhibit a longer decay time than greater than 10 keV hard X-rays. Such energy-dependent temporal evolution strongly resembles the properties of large flares.

By examining the time profiles of the analyzed microflares, we find that, like big flares, microflares can also be roughly grouped into impulsive events and gradual events. The impulsive events, for instance, the events shown in Figures 9 and 10, exhibit a fast rise on timescales of a few seconds, and the time lag of low-energy emission with respect to higher energy emission is rather pronounced. On the other hand, the events around 16:34 UT on May 2 (Fig. 11) and at 17:17 UT on July 15 (Fig. 12) are relatively gradual with a rise time on the scale of several tens of seconds to a few minutes. These events do not exhibit a pronounced delay of lower energy emission with respect to higher energy emissions, and the time profiles of microwaves and up to 10 keV hard X-rays are similar to time profiles of soft X-rays. The spectral analysis of the limited samples (§ 4.2) is not enough to yield a noticeable difference in the hard X-ray and microwave spectral index between the two groups of events. In a future study, imaging of microflares

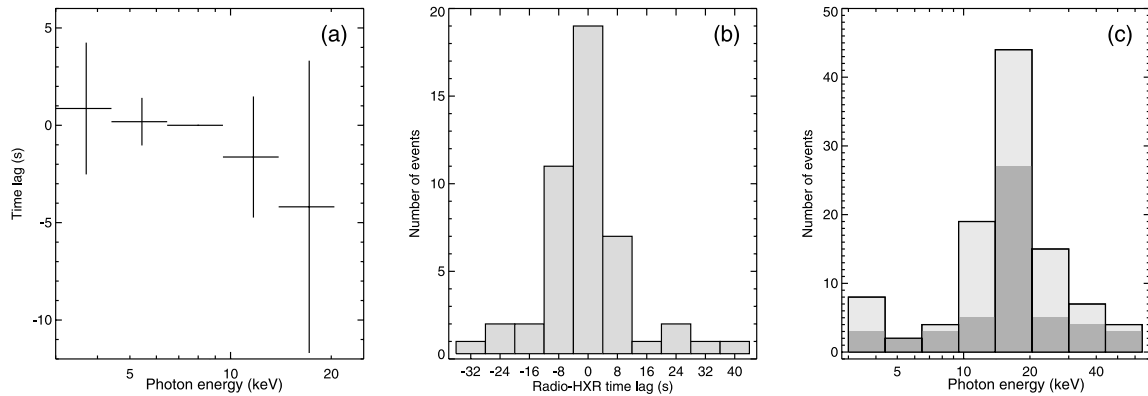


FIG. 13.—(a) Mean time lags of *RHESSI* X-rays at varying energies with respect to emission at 6–9 keV derived from 125 events. The horizontal bars denote the energy bins, and the vertical bars indicate the 1σ uncertainty. (b) Microflare distribution (total number of 50) of time lags of microwave time profiles (at peak frequencies) with respect to X-rays at 12–25 keV. (c) Neupert effect in microflares. The histogram in light gray (dark gray) shows the number of microflares vs. photon energies at which hard X-rays are best correlated with the time derivative of *GOES* 1–8 Å soft X-rays, with a greater than zero (≥ 0.5) cross-correlation coefficient.

should be incorporated to understand whether there is a physically significant difference between impulsive and gradual events.

Although the studied events are very small A- and B-class events, most of them exhibit complicated temporal structures of a few seconds in both hard X-rays and microwaves. All the events shown in this paper have multiple peaks in hard X-rays and microwaves. Note that these multiple peaks are reproduced in the time derivative of *GOES* 1–8 Å soft X-ray emissions. Such observations suggest that the microflares considered in this paper each consist of a group of bursts at even smaller scales, in terms of burst duration, that should be regarded as separate energy releases. With this fact in mind, the number of microflares can be raised by a few times.

It is of particular interest to compare the time derivative of soft X-rays with emissions at higher energies that are presumably of nonthermal nature. The so-called Neupert effect (Neupert 1968), namely, the time integral of hard X-ray or microwave emission is correlated with the soft X-ray light curve, has been reported in many major flares (e.g., Dennis & Zarro 1993), including flares observed by *RHESSI* (Dennis et al. 2003). This is interpreted as an indication that released energy in flares is primarily carried by nonthermal particles that subsequently heat plasmas to produce soft X-ray emissions.

Noting that, in many events, the multiple peaks in hard X-rays and microwaves are visible in the time derivative of soft X-rays (Fig. 9a–12a), we make a simple examination of the energy-dependent Neupert effect in microflares. For each of the 125 events, we cross-correlate the time derivative of *GOES* 1–8 Å soft X-rays with the *RHESSI* light curves in a few energy ranges from 3 to 60 keV and record the energy ϵ_N that yields the highest correlation coefficient ρ . In Figure 13c we plot the ϵ_N distribution, showing that the correlation resulting from the Neupert effect is greatest in the photon energy range of 14–20 keV at which hard X-rays are more likely to be emitted by nonthermal electrons (also see § 4.2). Such a result is more pronounced if we only consider events with a significant correlation, for example, $\rho \geq 0.5$. This result corroborates that the Neupert effect is occurring in a considerable number of small-scale events at B-class level. However, the fact that the correlation peaks at 14–20 keV does not imply that the Neupert effect is absent for hard X-rays at higher energies. In most events in this study, there is no significant emission beyond 20 keV, and the small signal-to-noise ratio

above 20 keV results in the poor correlation. To draw a solid conclusion on whether the energy release in microflares is primarily nonthermal requires a thorough quantitative evaluation of thermal and nonthermal energies in these events through spectral analysis (Lee et al. 1995; Dennis et al. 2003).

4.2. X-Ray and Microwave Spectral Analysis

The *RHESSI* spectral analysis is conducted using SPEX software. We use a double power law plus thermal model (Krucker et al. 2002) and fit the free parameters of the lower energy cutoff (ϵ_l) of the double power law, the power-law index (γ) and flux normalization of the component above ϵ_l , and the temperature (T_e) and emission measure (EM) of the thermal component. The power-law index of the nonthermal component below ϵ_l is set to a fixed value of 1.5 (Krucker et al. 2002). The fits to several events are shown in Figures 9b–12b, each with $\frac{1}{3}$ keV spectral resolution, 4 s integration, an energy range of 3 to 20–30 keV at the peak times, and χ^2 of the fits between 1 and 2. At peak times, most of the events are better fitted with a power-law component dominating greater than 10 keV emissions, except the gradual event at 16:34 UT on May 2 (Fig. 12) that is virtually dominated by a thermal component.

Background subtraction is critical to spectral fitting. In most of the events, we subtract the values linearly interpolated from the preflare and postflare backgrounds. We found that different choices of background selection mostly affect the fit to the thermal component, or the low-energy component below 10 keV, but do not lead to significant changes to the fitting results of the nonthermal part of the spectrum. For the analysis to be reliable, the fits to all the shown events are performed using various backgrounds and by different individuals independently, and by comparing the fitting results, we are satisfied with the consistency of these results.

In Figures 9d–12d, we also show the microwave total power spectra of these events. They exhibit both the optically thick and optically thin emissions. Assuming that nonthermal electrons that emit microwaves have a power-law distribution $N(E) \sim N_0(E/E_0)^{-\delta}$, we use the approximation formula by Dulk & Marsh (1982) to compute the spectral index δ of the electrons as $\delta = (1.22 - \beta)/0.9$. The value of β is retrieved by fitting the optically thin part of the microwave spectrum to a power-law function $F(f) \sim f^{-\beta}$, where F is the total power flux and f is the frequency. Note that for the events shown in Figures 9–12, the distance between the OVSA pointing and the

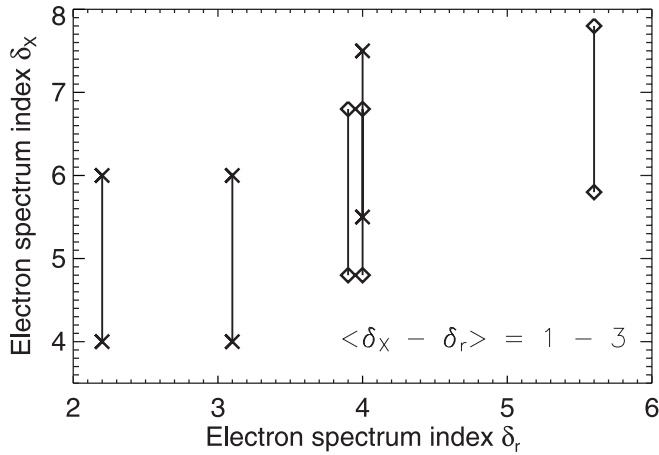


FIG. 14.—Scatter plot of the electron spectrum index δ_X derived from *RHESSI* photon spectrum fitting against the electron spectrum index δ_r derived from microwave spectrum fitting for six bursts shown in Figs. 9–12; δ_X is derived for both thick- and thin-target assumptions by $\delta_X = \gamma_X + 1.5$ and $\delta_X = \gamma_X - 0.5$, respectively, as indicated by the upper and lower symbols, respectively. The crosses and diamonds refer to impulsive and gradual bursts, respectively.

RHESSI source location is no more than $100''$, which does not distort the fitting results.

The hard X-ray and microwave spectra shown in Figures 9–12 clearly indicate emissions at these two wavelengths by nonthermal electrons at least at peak times. We note that in May and July, some tiny events with very low *GOES* absolute flux exhibit strong nonthermal components. An outstanding example is the microflare at 16:23 UT on July 14 (Fig. 10) in NOAA 30. Figure 1 shows the hard X-ray and microwave dynamical spectra of this event, confirming that the event consists of several peaks, all visible in fairly high energies and frequencies. In *GOES* categorization, it is a B7.8 event, and with background subtracted, its soft X-ray flux is B1.5. However, significant emissions can be detected by *RHESSI* at up to 30 keV in a couple of bursts. Among all the analyzed events, this event exhibits the hardest spectra as derived from both hard X-rays ($\gamma_X \approx 4.5$) and microwaves ($\delta_r \approx 2-4$).

We also compare the results of fitting hard X-ray and microwave spectra for the six bursts shown in Figures 9–12. The mean value of γ_X is 5.3 ± 0.7 , and the mean value of δ_r is 3.8 ± 1.2 . Note that γ_X is the power-law index of the hard X-ray photon spectrum, and the index of the electron spectrum can be either $\delta_X = \gamma_X + 1.5$ or $\delta_X = \gamma_X - 0.5$ depending on whether the hard X-rays are thick- or thin-target emission. Figure 14 shows the scatter plot of δ_X , in thick- and thin-target regimes, respectively, against δ_r for these six bursts. The two are roughly scaled, but in all events the electron spectrum derived from fitting the microwave total power spectrum is systematically harder than from fitting the hard X-ray photon spectrum. If nonthermal hard X-rays are emitted by thick-target sources, the mean difference between δ_X and δ_r is 3.0 ± 0.6 .

This discrepancy is substantially greater than that reported by Silva et al. (2000), who analyzed hard X-ray and microwave spectra of 57 large flares jointly observed by the *Solar Maximum Mission* and *OVSA* and derived a mean difference of 1.0 in the power-law index of electrons emitting hard X-rays and microwaves. Electrons emitting microwaves are thought to have a higher energy than electrons emitting hard X-rays (Nitta & Kosugi 1986; Kosugi et al. 1988). It was thus proposed that the electron spectrum hardens toward higher energies (Silva

et al. 2000), but it remains unclear where the high-energy break between two power-law distributions is. Recent results on *RHESSI* microflare spectra have suggested that nonthermal emissions in microflares have a steeper spectrum compared with major flares (Benz & Grigis 2003; Dennis et al. 2003). With a thick-target assumption, the spectral index of electrons emitting hard X-rays ranges from 6 to nearly 8 in the few events shown in this paper, which agrees with the notion above. On the other hand, the microflare electron spectrum inferred from the microwave total power spectrum is as hard as for large flares. Therefore, the great discrepancy would hint at an acceleration mechanism that sharpens the difference between the low-energy and high-energy electron spectrum by further “softening” electrons emitting hard X-rays in microflares.

5. CONCLUSIONS

We conduct a preliminary study on microflares that are detected in 12–25 keV hard X-ray observations by *RHESSI* and microwave observations by *OVSA*. These events, amounting to 760 in number observed during *RHESSI* open-shutter mode from 2002 May through September, have a mean *GOES* flux at the B2.0 level with the background subtracted and represent relatively large microflares compared with the even smaller events that can be detected by *RHESSI* in lower energy ranges, as reported by Krucker et al. (2002) and Benz & Grigis (2002). The statistical characteristics of these events are investigated in comparison with numerous previous studies. We also analyze hard X-ray and microwave data for several tens of events that are identified in observations by both instruments. The properties of microflares are also compared with major flares.

Our results show that the peak count rates of the hard X-ray bursts have a power-law distribution with an index of 1.75 ± 0.03 . The flux distribution of soft X-ray counterparts, observed by *GOES* at 1–8 Å, of these *RHESSI* bursts also agrees with previous results (Veronig et al. 2002 and references therein).

Like major flares, the occurrence of the microflare events considered in this study is correlated with the solar activity represented by *GOES* soft X-ray flux; in other words, when the Sun is more active with a higher soft X-ray flux level, more microflare events are produced. Judging from coordinated microwave observations and limited imaging of *RHESSI* bursts, most events in this study are probably produced by active regions; however, microflares are not equally distributed over all active regions. Some active regions are more productive than other regions, and the productivity of a certain active region is associated with its magnetic configuration, as in the case for large flares. While some active regions that dominate other regions during their disk passage are productive in both very small and very large events, we also find an active region that produces many small-scale events but does not produce very big flares over M class. A possible scenario might be that the frequent occurrence of small-scale events in this region helps relax the configuration and prevent it from building up large events. To check this possibility, a quantitative analysis of the energy budget in these small-scale events should be conducted in a future study. Further studies on active region evolution may shed light on whether there is a fundamental difference between active regions that perform differently in producing small- and large-scale events and what the implications will be for space weather forecasts.

Most of the microflares are detected in hard X-rays at over 10 keV, and about 40% of the analyzed events that are

jointly observed by *RHESSI* and *OVSA* are visible as microwave bursts with a peak flux of 1–10 sfu. Particularly, the two large antennas in *OVSA* can unambiguously detect bursts with a flux below 1 sfu. Most *RHESSI* microflares that occur within the FOV of *OVSA* large antennas are detected by *OVSA* large antennas that usually target active regions. The energy-dependent temporal evolution in microwaves and X-rays exhibits properties that strongly resemble flares at larger scales. Albeit small, many microflare events exhibit complicated temporal structures with multiple peaks in hard X-rays and microwaves, which are reproduced in the time derivative of soft X-rays. The Neupert effect seen in many large flares is also evident in microflares, and our analysis of over 100 events shows that the soft X-ray time derivative is well correlated with hard X-rays above 10 keV in one-half the events.

The “nonthermality” of microflares reflected in microwaves and hard X-rays does not necessarily depend on the solar activity level. We find that some small events with very low soft X-ray flux exhibit strong nonthermal emission in hard X-rays of over 20 keV and microwaves at over 10 GHz with a power-law electron spectral index as low as 2. The analysis also reveals the intriguing finding that there is a large discrepancy in the electron spectral index derived from hard X-ray photon spectra and from microwave total power spectra. The difference amounts to 3.0 compared with 1.0 acquired from large flares. Should we expect the hard X-ray-emitting low-energy electrons in microflares to become significantly “softened” by an acceleration or scattering mechanism, and if so, why? We also note that the lower and higher energy cutoffs, given their importance in accurate evaluation of the energy budget and acceleration mechanism, have remained a riddle for decades. Will the microflare spectral properties in X-rays and microwaves be accounted for by a thorough spectral analysis taking into consideration the appropriate energy cutoffs (e.g., Holman 2003)?

The results and questions raised from this preliminary study deserve more consideration and further in-depth investigation.

We are still far from being able to answer the question of whether microflares can account for heating of the active region corona. First, the occurrence rate (events per hour) derived in this preliminary study is greatly underestimated in comparison with previous reports (Benz & Grigis 2003 and references therein). It is most likely that many weak events were missed by the *RHESSI* burst catalog in the energy range of 12–25 keV, which also explains the steep flux distribution of *RHESSI* burst-related soft X-ray events in the low-flux range below the rollover (Fig. 4a). A careful inspection of the original data down to 3 keV is required to obtain a closer estimate of the event occurrence rate, as well as the frequency distribution in the low-flux/counts domain. A more sophisticated issue is the derivation of the energy distribution of microflares through adequately precise spectral analysis on a good number of events, which is also crucial to understanding the thermal or nonthermal nature of the primary energy release in microflares (e.g., Dennis et al. 2003). Such an accomplishment will require assiduous and collaborative effort by teams with a common interest.

The authors acknowledge the *RHESSI* team for operating the instrument and providing efficient data and software service. We greatly appreciate constructive comments and suggestions by the referee, Sam Krucker. J. Q. thanks Gordon Holman, Linhui Sui, Brian Dennis, and the *RHESSI* team at GSFC/NASA for their hospitality during her visit and Hugh Hudson, Jim McTiernan, and Kim Torbelt for help with the data and software. This work is supported by NASA grants NAG5-10212 and NAG5-12782. *OVSA* is supported by NSF grant AST 03-07670 to New Jersey Institute of Technology. This study includes data from the synoptic program at the 150 foot Solar Tower of the Mount Wilson Observatory operated by UCLA and from the solar Active Region Monitor program maintained by Peter T. Gallagher.

REFERENCES

- Aschwanden, M. J. 1999, *Sol. Phys.*, 190, 233
 Bastian, T. S. 1991, *ApJ*, 370, L49
 Benz, A. O., & Grigis, P. C. 2002, *Sol. Phys.*, 210, 431
 ———. 2003, *Adv. Space Res.*, 32, 1035
 Berghmans, D., McKenzie, D., & Clette, F. 2001, *A&A*, 369, 291
 Canfield, R. C., & Metcalf, T. R. 1987, *ApJ*, 321, 586
 Crosby, N. B., Aschwanden, M. J., & Dennis, B. R. 1993, *Sol. Phys.*, 143, 275
 Dennis, B. R., Veronig, A., Schwartz, R. A., Sui, L., Tolbert, A. K., & Zarro, D. M. 2003, *Adv. Space Res.*, 32, 2459
 Dennis, B. R., & Zarro, D. M. 1993, *Sol. Phys.*, 146, 177
 Dulk, G. A., & Marsh, K. A. 1982, *ApJ*, 259, 350
 Feldman, U., Doschek, G. A., & Klimchuk, J. A. 1997, *ApJ*, 474, 511
 Garaimov, V. I., Kundu, M. R., & Grigis, P. C. 2003, *BAAS*, 35(3), 16.03
 Gary, D. E., Hartl, M., & Shimizu, T. 1997, *ApJ*, 477, 958
 Gary, D. E., & Hurford, G. J. 1990, *ApJ*, 361, 290
 Gopalswamy, N., Payne, T. E. W., Schmahl, E. J., Kundu, M. R., Lemen, J. R., Strong, K. T., Canfield, R. C., & de La Beaujardiere, J. 1994, *ApJ*, 437, 522
 Holman, G. D. 2003, *ApJ*, 586, 606
 Hurford, G. J., et al. 2002, *Sol. Phys.*, 210, 61
 Kosugi, T., Dennis, B. R., & Kai, K. 1988, *ApJ*, 324, 1118
 ———. 2000, *Sol. Phys.*, 191, 341
 Krucker, S., Benz, A. O., Bastian, T. S., & Acton, L. W. 1997, *ApJ*, 488, 499
 Krucker, S., Christe, S., Lin, R. P., Hurford, G. J., & Schwartz, R. A. 2002, *Sol. Phys.*, 210, 445
 Kucera, T. A., Dennis, B. R., Schwartz, R. A., & Shaw, D. 1997, *ApJ*, 475, 338
 Lee, T. T., Petrosian, V., & McTiernan, J. M. 1995, *ApJ*, 448, 915
 Lin, R. P., Schwartz, R. A., Kane, S. R., Pelling, R. M., & Hurley, K. C. 1984, *ApJ*, 283, 421
 Lin, R. P., et al. 2002, *Sol. Phys.*, 210, 3
 Liu, C., Qiu, J., Gary, D. E., Krucker, S., & Wang, H. 2004, *ApJ*, 604, 442
 Neupert, W. M. 1968, *ApJ*, 153, L59
 Nita, G. M., Gary, D. E., Lanzerotti, L. J., & Thomson, D. J. 2002, *ApJ*, 570, 423
 Nita, G. M., Gary, D. E., & Lee, J. 2004, *ApJ*, 605, 528
 Nitta, N. 1997, *ApJ*, 491, 402
 Nitta, N., & Kosugi, T. 1986, *Sol. Phys.*, 105, 73
 Parker, E. N. 1983, *ApJ*, 264, 635
 Porter, J. G., Moore, R. L., Reichmann, E. J., Engvold, O., & Harvey, K. L. 1987, *ApJ*, 323, 380
 Qiu, J., Wang, H., Chae, J., & Goode, P. R. 1999, *Sol. Phys.*, 190, 153
 Rauscher, E., Christe, S., Hannah, I., Krucker, S., & Lin, R. P. 2003, AGU Fall Meeting 2002, abs. SH21B-0167
 Shimizu, T. 1995, *PASJ*, 47, 251
 Shimizu, T., Shine, R. A., Title, A. M., Tarbell, T. D., & Frank, Z. 2002, *ApJ*, 574, 1074
 Shimizu, T., Tsuneta, S., Acton, L. W., Lemen, J. R., Ogawara, Y., & Uchida, Y. 1994, *ApJ*, 422, 906
 Silva, A. V. R., Wang, H., & Gary, D. E. 2000, *ApJ*, 545, 1116
 Simnett, G. M., Mouradian, Z., Martres, M.-J., & Soru-Escout, I. 1989, *A&A*, 224, 284
 Smith, D. 2002, Behind, Beneath, and Before *RHESSI* Spectroscopy (Greenbelt: NASA), <http://hesperia.gsfc.nasa.gov/rhessidatacenter/instrument/doc4.pdf>
 Veronig, A., Temmer, M., Hanslmeier, A., Otruba, W., & Messerotti, M. 2002, *A&A*, 382, 1070
 Wang, H., Chae, J., Qiu, J., Lee, C. Y., & Goode, P. R. 1999, *Sol. Phys.*, 188, 365
 White, S. M., Kundu, M. R., Shimizu, T., Shibasaki, K., & Enome, S. 1995, *ApJ*, 450, 435
 Zirker, J. B. 1993, *Sol. Phys.*, 148, 43